Supplementary Information

Cost-Effective Hydrotalcite-Derived Fe-Based Catalysts for Stable and Continuous Catalytic Methane Decomposition

Xiaoxin Li[1], Shuzhi Zhao[2], Chao Deng[1], Rong Chen[1], Furong Xie[1], Zinan Wu[1], Zifeng Ma[2,*], Guo-Ming Weng[1,*]

[1] Shanghai Key Laboratory of Hydrogen Science & Center of Hydrogen Science, School of Materials Science and Engineering, Shanghai Jiao Tong University, Shanghai 200240 P. R. China

[2] Shanghai Electrochemical Energy Devices Research Center, School of Chemistry and Chemical Engineering, Shanghai Jiao Tong University, Shanghai 200240, China

* Email: zfma@sjtu.edu.cn; guoming.weng@sjtu.edu.cn

Chemicals and materials

Ferrous chloride tetrahydrate ($FeCl_2$•$4H_2O$, 99%), Ferric nitrate nonahydrate ($Fe(NO_3)_3$•$9H_2O$, and Sodium hydroxide (NaOH, ≥ 96%), were purchased from Sinopharm Chemical reagent Co., Ltd. Aluminium nitrate nonahydrate ($Al(NO_3)_3$•$9H_2O$, 99.5%) was obtained from Anhui Senrise Technologies Co., Ltd. Sodium carbonate (Na_2CO_3, 99.8%) was purchased from General-reagent. Alumina (γ-Al_2O_3, 20nm, ≥ 99.99%) was obtained from Shanghai aladdin Biochemical Technology Co., Ltd. Deionized water was obtained from a Water Purifier apparatus (Hitech, PF-10D). All reagents were used without further purification.

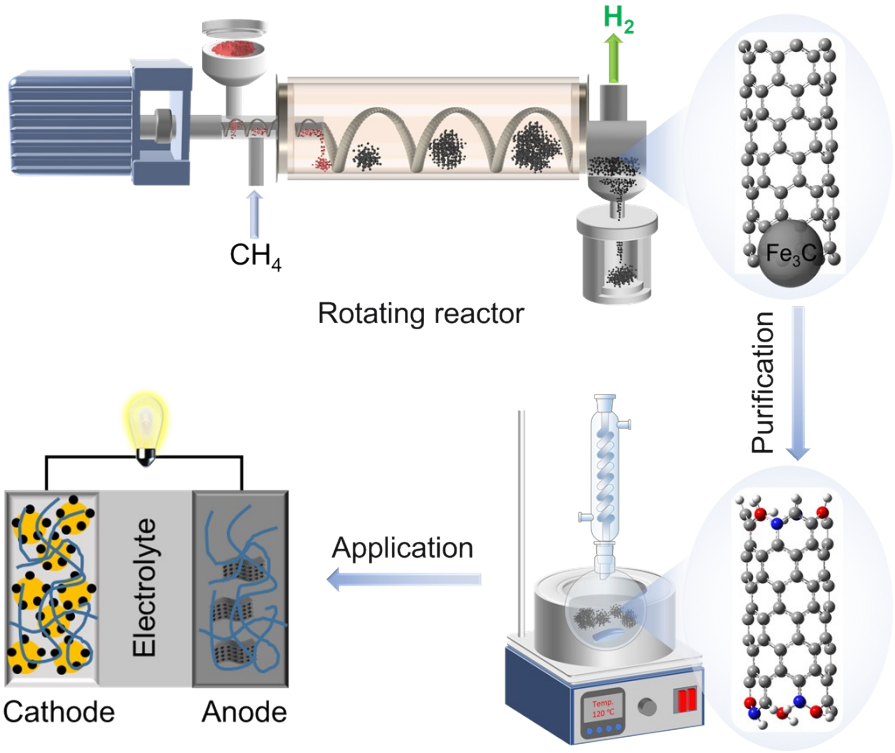

Figure S1. The concept of a rotating reactor (ref. 1) for continuous CMD combined with the purification and battery application of carbon products.

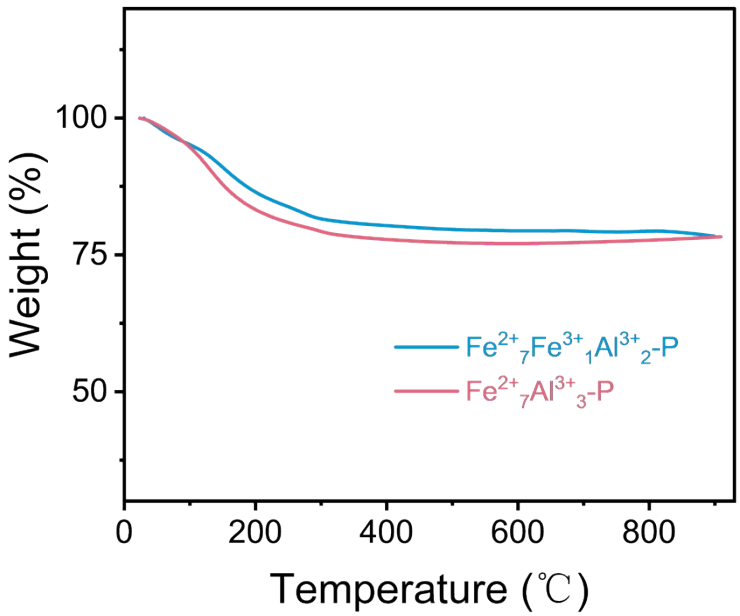

Figure S2. TGA of precursors. $Fe^{2+}_{7}Al^{3+}_{3}$-P (red plot); $Fe^{2+}_{7}Fe^{3+}_{1}Al^{3+}_{2}$-P (blue plot). The precursors were heated from room temperature to 900 ℃ with a heating rate of 5 ℃ min^{-1} under air condition.

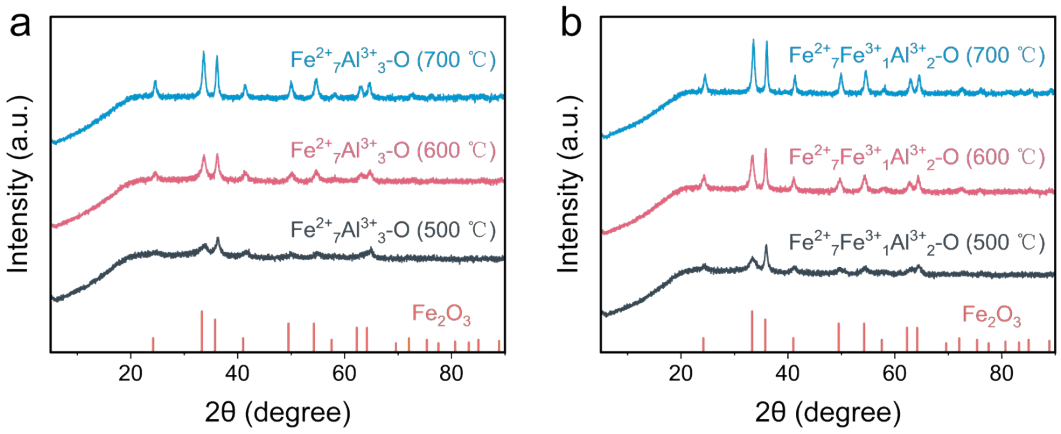

Figure S3. (a) and **(b)** are XRD patterns of $Fe^{2+}_7Al^{3+}_3$-O and $Fe^{2+}_7Fe^{3+}_1Al^{3+}_2$-O at different calcination temperatures (i.e., 500, 600 and 700 ℃), respectively.

Table S1. Summary of Fe_2O_3 crystal size corresponding to corresponding to Figure S3.

Catalyst	Fe_2O_3 crystal sized (nm)
$Fe^{2+}_7Al^{3+}_3$-O (600 ℃)	16.7
$Fe^{2+}_7Al^{3+}_3$-O (700 ℃)	17.4
$Fe^{2+}_7Fe^{3+}_1Al^{3+}_2$-O (600 ℃)	18.2
$Fe^{2+}_7Fe^{3+}_1Al^{3+}_2$-O (700 ℃)	22.3

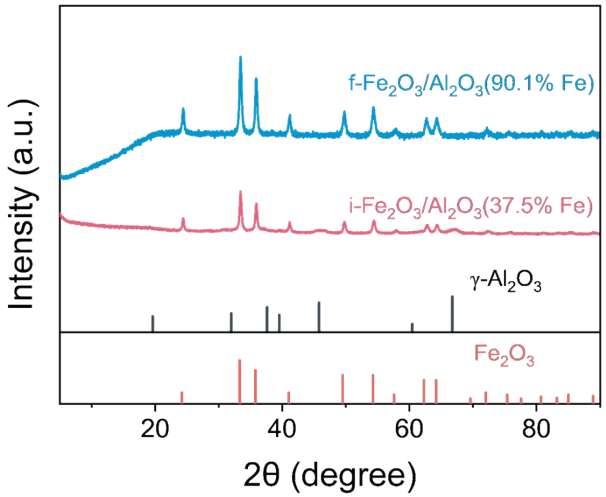

Figure S4. XRD patterns of Fe-based catalyst synthesized by impregnation (i-Fe_2O_3/Al_2O_3 (37.5% Fe)) and fusion method (f-Fe_2O_3/Al_2O_3 (90.1% Fe)).

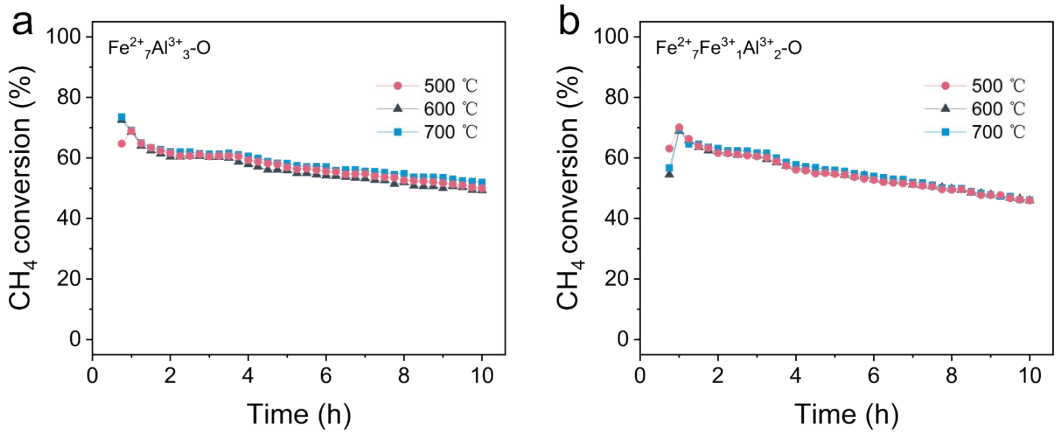

Figure S5. **(a)** and **(b)** are CH_4 conversion efficiency of $Fe^{2+}{}_7Al^{3+}{}_3$-O and $Fe^{2+}{}_7Fe^{3+}{}_1Al^{3+}{}_2$-O, respectively, generated from different calcination temperatures.

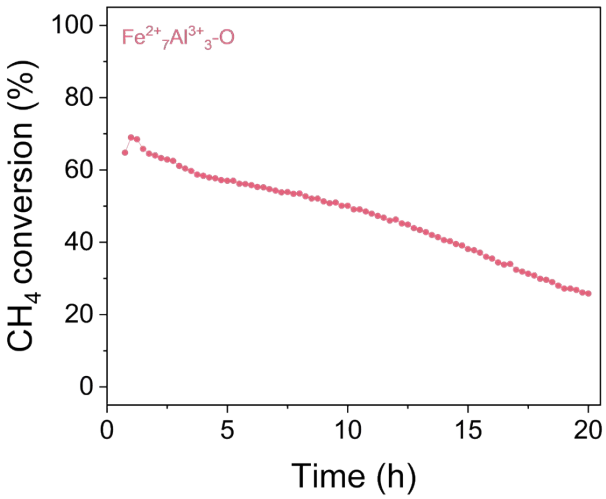

Figure S6. CH_4 conversion efficiency of $Fe^{2+}{}_7Al^{3+}{}_3$-O at reaction temperature of 730 ℃ under 4 sccm for 20 h.

Table S2. Summary of CMD conditions for Figure S5, Figure S6, and Figure 5.					
Catalyst	**Weigh t (g)**	**Carbon Products (g)**	**Temp. (℃)**	**Reduction gas & reaction gas (sccm)**	**Space velocity (L h^{-1} g^{-1})**
$Fe^{2+}_7Al^{3+}_3$-O	0.1	0.4689	850	4/CH_4	2.4
		0.6456	800		
		0.9424	750		
		0.9509	730		
		1.4002	730 (20h)		
		0.9315	710		
		0.6237	650		
$Fe^{2+}_7Al^{3+}_3$-O	0.2 g	1.0296	730		1.2
$Fe^{2+}_7Al^{3+}_3$-O	0.05	0.7725	730		4.8
$Fe^{2+}_7Al^{3+}_3$-O (600 ℃)	0.1	0.9615	730		2.4
$Fe^{2+}_7Al^{3+}_3$-O （700 ℃)	0.1	0.9787	730		2.4
$Fe^{2+}_7Fe^{3+}_1Al^{3+}_2$-O	0.1	0.5432	850		2.4
		0.5085	800		
		0.8522	750		
		0.9260	730		
		0.8865	710		
		0.6851	650		
$Fe^{2+}_7Fe^{3+}_1Al^{3+}_2$-O	0.2 g	1.0697	730		1.2
$Fe^{2+}_7Fe^{3+}_1Al^{3+}_2$-O	0.05	0.7020	730		4.8
$Fe^{2+}_7Fe^{3+}_1Al^{3+}_2$-O (600 ℃)	0.1	0.9043	730		2.4
$Fe^{2+}_7Fe^{3+}_1Al^{3+}_2$-O (700 ℃)	0.1	0.9170	730		2.4

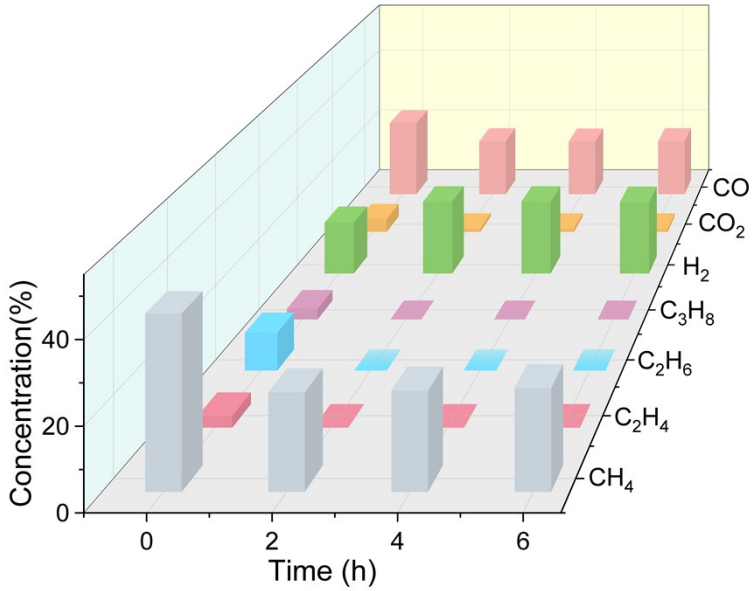

Figure S7. The three-dimensional bar char depicting the variation of different components in mixed gas, at reaction time of 0, 2, 4, and 6 h. The experiment was perform using 0.1 g $Fe^{2+}_7Al^{3+}_3$-O as catalyst at 730 ℃, with mixed gas flow rate of 4 sccm.

Table S3. The carbon products and concentration of various components in mixed gas at different reaction time corresponding to **Figure S7.**

Gas	**Concentration (0 h, %)**	**Concentration (2 h, %)**	**Concentration (4 h, %)**	**Concentration (6 h, %)**
CH_4	42	23.4	23.8	24.4
C_2H_4	3	0	0	0
C_2H_6	10	0	0	0
C_3H_8	3	0	0	0
H_2	15	21.1	21.1	21
CO_2	4	1	1	1
CO	23	17.1	17	17.1
Carbon products: 0.4924 g				

Note: The gas samples were qualified and quantified by GC-MS (gas chromatograph-mass spectrometer).

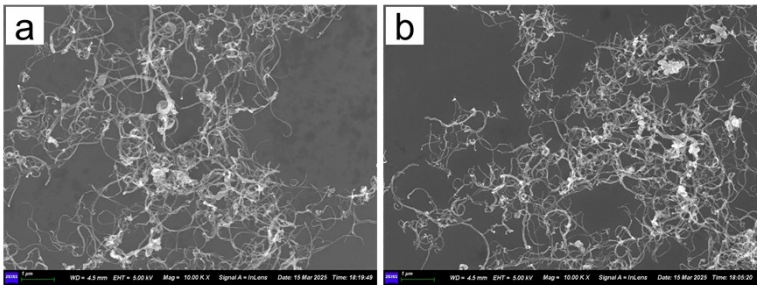

Figure S8. Low-magnification SEM images of **(a)** CNT ($Fe^{2+}_7Al^{3+}_3$-O) and **(b)** CNT ($Fe^{2+}_7Fe^{3+}_1Al^{3+}_2$-O)

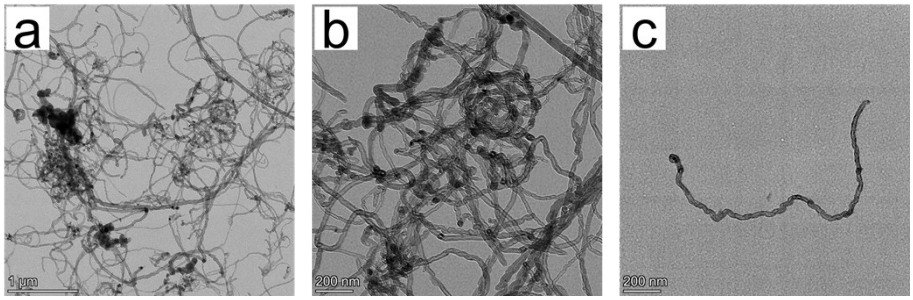

Figure S9. (a), **(b)** and **(c)** TEM images of CNT (Fe^{2+}_7 $Fe^{3+}_1Al^{3+}_2$-O) at different magnification scales, respectively.

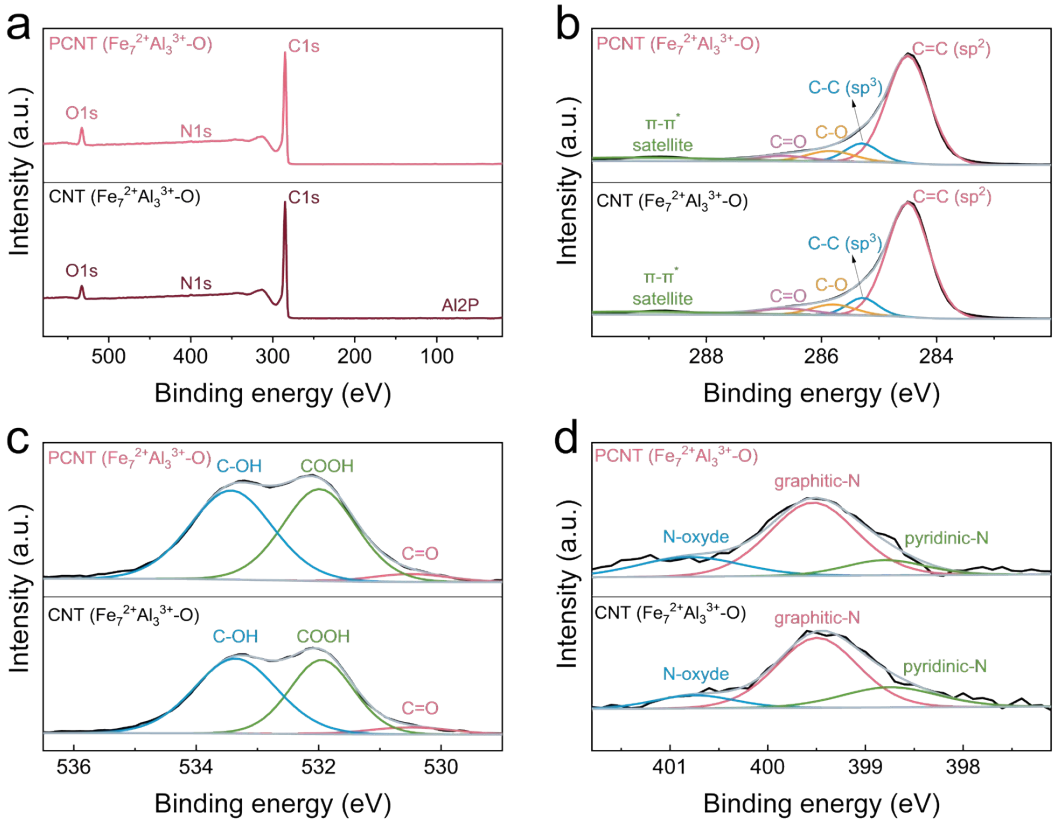

Figure S10. (a) XPS survey spectra of CNT ($Fe^{2+}_7Al^{3+}_3$-O) and PCNT ($Fe^{2+}_7Al^{3+}_3$-O). **(b)**, **(c)** and **(d)** are high resolution XPS spectra of C 1s, O 1s, and N 1s, respectively, for CNT ($Fe^{2+}_7Al^{3+}_3$-O) and PCNT ($Fe^{2+}_7Al^{3+}_3$-O).

Table S4. The relative concentration (atomic percentage, at%) of different elements in CNT (commercial), CNT ($Fe^{2+}_7Al^{3+}_3$-O) and PCNT ($Fe^{2+}_7Al^{3+}_3$-O).

Element / Carbon	C1s	N1s	O1s	Al2P	Fe2p
CNT (commercial) [2]	97.48	0.20	2.33	0	0
CNT ($Fe^{2+}_7Al^{3+}_3$-O)	94.25	0.44	5.08	0.23	0
PCNT ($Fe^{2+}_7Al^{3+}_3$-O)	92.98	0.42	6.60	0	0

Table S5. Binding energy and the relative concentration (at%) of C species in the CNT ($Fe^{2+}_7Al^{3+}_3$-O) and PCNT ($Fe^{2+}_7Al^{3+}_3$-O).

Group	C-C (sp^2)	C-C (sp^3)	C=O	C-O	π=π^* satellite
Binding Energy (eV)	284.5	285.3	285.8	286.6	289.2
relative concentration (at%) CNT($Fe^{2+}_7Al^{3+}_3$-O)	67.91	7.65	6.61	5.09	6.96
relative concentration (at%) PCNT($Fe^{2+}_7Al^{3+}_3$-O)	65.59	8.87	7.06	5.14	6.22

Table S6. Binding energy and the relative concentration (at%) of O species in the CNT ($Fe^{2+}_7Al^{3+}_3$-O) and PCNT ($Fe^{2+}_7Al^{3+}_3$-O).

Group	C=O	COOH	C-OH
Binding Energy (eV)	530.5	532.0	533.4
relative concentration (at%) CNT($Fe^{2+}_7Al^{3+}_3$-O)	0.25	2.06	2.69
relative concentration (at%) PCNT($Fe^{2+}_7Al^{3+}_3$-O)	0.26	2.98	3.23

Table S7. Binding energy and the relative concentration (at%) of N species in the CNT ($Fe^{2+}_7Al^{3+}_3$-O) and PCNT ($Fe^{2+}_7Al^{3+}_3$-O).

Group	Pyridinic-N	Graphitic-N	N-oxide
Binding Energy (eV)	398.8	399.5	400.8
relative concentration (at%) CNT($Fe^{2+}_7Al^{3+}_3$-O)	0.09	0.27	0.05
relative concentration (at%) PCNT($Fe^{2+}_7Al^{3+}_3$-O)	0.06	0.30	0.1

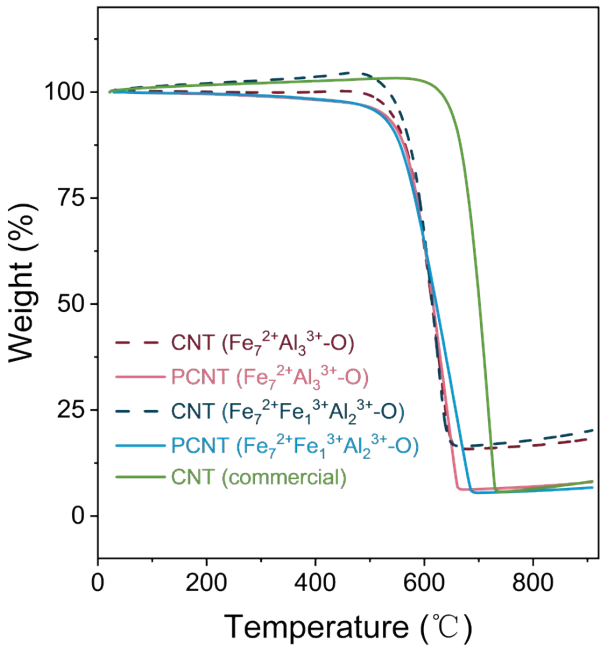

Figure S11. Thermogravimetric analysis (TGA) of various CNTs. The samples were heated from room temperature at a rate of 10 ℃ min^{-1} under air condition.

Table S8. Structural properties of Carbon products from CH_4 decomposition.

Carbon products	I_D/I_G	Specific surface area (m^2 g^{-1})	Pore diameter (nm)	Total pore volume (cm^3 g^{-1})
CNT [2] (Previous work)	1.11	269.375	2.897	0.613
PCNT ($Fe^{2+}_7Al^{3+}_3$-O)	0.64	80.2	3.827	0.399

Table S9. Fitting EIS results of the as-prepared NFS//Na half cells

Conduct	Number of cycles	R_{ohm} (Ω)	R_{SEI} (Ω)	R_{CT} (Ω)
CNT (commercial)	0	3.79	8.55	4.63
CNT (commercial)	127	8.50	42.24	20.4
PCNT ($Fe^{2+}_7Al^{3+}_3$-O)	0	3.12	13.47	7.27
PCNT ($Fe^{2+}_7Al^{3+}_3$-O)	127	7.90	41.84	21.59

Table S10. Comparison of electrical conductivity with CNT (commercial), CNT($Fe^{2+}_7Al^{3+}_3$-O), and PCNT($Fe^{2+}_7Al^{3+}_3$-O).

Samples	Conductivity (S cm^{-1})	Weight of sample (g)	Specific conductivity (S cm^2 g^{-1})
CNTs (commercial)	12.32	0.0394	3983.3
CNTs ($Fe^{2+}_7Al^{3+}_3$-O)	10.57 6.531（2）	0.0477 0.0436（2）	2822.8 1908.2（2）
PCNTs ($Fe^{2+}_7Al^{3+}_3$-O)	20.34 8.598（2）	0.0585 0.0468（2）	4429.2 2512.1（2）

Notes: The electrical conductivity test results for powder samples are dependent on the density of the table-shaped test samples and the pressure applied during their formation (i.e., two of the important factors). The data displayed in green are those from repeated experiments.

References

(1) Yan, P.; Zhang, K.; Peng, Y. Study of Fe_2O_3-Al_2O_3 catalyst reduction parameters and conditions for catalytic methane decomposition. *Chemical Engineering Science* **2022**, *250*, 117410. DOI: 10.1016/j.ces.2021.117410.

(2) Wu, Z.; Li, X.; Xie, F.; Chen, R.; Deng, C.; Weng, G.-M. Sustainable pyrolytic carbon negative electrodes for sodium-ion batteries. *Journal of Power Sources* **2024**, *621*. DOI: 10.1016/j.jpowsour.2024.235262.